Boron nitride quantum dots decorated ultrathin porous g-C$_3$N$_4$: Intensified exciton dissociation and charge transfer for promoting visible-light-driven molecular oxygen activation

Yang Yang[a,b,1], Chen Zhang[a,b,1], Danlian Huang[a,b,1], Guangming Zeng[a,b,*], Jinhui Huang[a,b,*], Cui Lai[a,b], Chengyun Zhou[a,b], Wenjun Wang[a,b], Hai Guo[a,b], Wenjing Xue[a,b], Rui Deng[a,b], Min Cheng[a,b], Weiping Xiong[a,b]

[a] *College of Environmental Science and Engineering, Hunan University, Changsha, 410082, PR China*
[b] *Key Laboratory of Environmental Biology and Pollution Control, Ministry of Education, Hunan University, Changsha 410082, PR China*

ARTICLE INFO

ABSTRACT

Graphitic carbon nitride (g-C$_3$N$_4$) has enormous potential for photocatalysis, but only possesses moderate activity because of excitonic effects and sluggish charge transfer. Herein, metal-free heterostructure photocatalyst constructed by boron nitride quantum dots (BNQDs) and ultrathin porous g-C$_3$N$_4$ (UPCN) was successfully developed for overcoming these defects. Results showed that the BNQDs loaded UPCN can simultaneously promote the dissociation of excitons and accelerate the transfer of charges owing to the negatively charged functional groups on the surface of BNQDs as well as the ultrathin and porous nanostructure of g-C$_3$N$_4$. Benefiting from the intensified exciton dissociation and charge transfer, the BNQDs/UPCN (BU) photocatalyst presented superior visible-light-driven molecular oxygen activation ability, such as superoxide radical ($^{\cdot}$O$_2^-$) generation and hydrogen peroxide (H$_2$O$_2$) production. The average $^{\cdot}$O$_2^-$ generation rate of the optimal sample (BU-3) was estimated to be 0.25 μmol L^{-1} min^{-1}, which was about 2.3 and 1.6 times than that of bulk g-C$_3$N$_4$ and UPCN. Moreover, the H$_2$O$_2$ production by BU-3 was also higher than that of bulk g-C$_3$N$_4$ (22.77 μmol L^{-1}) and UPCN (36.13 μmol L^{-1}), and reached 72.30 μmol L^{-1} over 60 min. This work reveals how rational combination of g-C$_3$N$_4$ with BNQDs can endow it with improved photocatalytic activity for molecular oxygen activation, and provides a novel metal-free and highly efficient photocatalyst for environmental remediation and energy conversion.

1. Introduction

On the journey to develop green and sustainable technology to resolve global problems of environmental pollution and energy shortage, photocatalytic activating molecular oxygen to superoxide radical ($^{\cdot}$O$_2^-$) and hydrogen peroxide (H$_2$O$_2$) is deemed to be an ideal way [1–5]. On the one hand, molecular oxygen activation can be acquired by solar energy in the presence of proper photocatalyst wherein oxygen is reduced by photo-excited electrons [6–8]. On the other hand, $^{\cdot}$O$_2^-$ and H$_2$O$_2$ are all versatile clean oxidant for environmental remediation, while H$_2$O$_2$ is also a promising clean energy which can be applied for electricity generation in single compartment cells [9–11]. Therefore, it is of great interest to exploit solar energy to realize molecular oxygen activation, particularly in view of the environmental cost [12,13].

Nevertheless, the lack of efficient, stable, green and inexpensive catalysts for such photocatalytic molecular oxygen activation remains a principal issue [14,15].

Graphitic carbon nitride (g-C$_3$N$_4$), as a typical metal-free polymeric semiconductor, has been regarded as ideal photocatalyst in molecular oxygen activation owing to its merits of environmental benignity, facile synthesis, visible light response and excellent physicochemical stability [9,16]. Hirai and co-workers [16] found that g-C$_3$N$_4$ has a great potential to produce H$_2$O$_2$ under visible light irradiation. Zhang et al. [17] reported that molecular oxygen can be activated from visible light of semicrystalline carbon nitride containing abundant order-disorder interfaces. Wang's group [10] demonstrated that the combination of black phosphorus with polymeric carbon nitride significantly promotes the photocatalytic activation of molecular oxygen ($^{\cdot}$O$_2^-$ evolution and

H_2O_2 production). However, bulk g-C_3N_4 only exhibits moderate photocatalytic activity in most cases for two well-known reasons. Firstly, bulk g-C_3N_4 normally generates plenty of Frenkel excitons during photoexcitation process [18]. Due to the strong Coulomb interaction between Frenkel exciton, bulk g-C_3N_4 presents high exciton binding energy, resulting in slow exciton dissociation and serious charge recombination [17,19]. Secondly, because of the small specific surface area of bulk g-C_3N_4, even if the excitons split to free charges, the transfer of charges will be hindered [20]. And insufficient reaction active sites on the surface of g-C_3N_4 may also leads to the sluggish reaction kinetics. To address these challenges, various strategies have been exploited to promote the photocatalytic performance of bulk g-C_3N_4 [21–23].

Construction of nanostructures with special shapes, especially two-dimensional (2D) ultrathin and porous nanostructures, is considered to be an effective method to improve the photocatalytic activity of bulk g-C_3N_4 [24,25]. In comparison with bulk g-C_3N_4, ultrathin porous g-C_3N_4 has shorter diffusion pathways and higher specific surface area, which accelerate the dissociation of excitons and the transfer of free charges, and provide more active sites. Hence many attempts have been made to develop highly efficient ultrathin porous g-C_3N_4. Zhu et al. [26] prepared single atomic layer structured g-C_3N_4 nanosheets through chemical exfoliation method, promoting the transfer and separation of photo-generated charge carrier. Tian et al. [27] adopted precursor-reforming strategy to synthesize the mesoporous ultrathin g-C_3N_4, which enhanced the photocatalytic activity toward hydrogen production. Recently, our group synthesized a series of g-C_3N_4 with ultrathin and porous nanostructures, which exhibited significantly improved visible-light-driven photocatalytic performance for environmental remediation owing to the large specific surface area and efficient exciton dissociation as well as charge transfer [28,29].

Beside microstructure modulation, implanting g-C_3N_4 with non-metal materials (for example, graphene [30], carbon quantum dots [31], black phosphorus [10] and hexagonal boron nitride [32]) has also been widely investigated to elevate the photocatalytic activity. Hexagonal boron nitride (h-BN), known as "white graphene", possesses some peculiar properties including low toxicity, high chemical and thermal stability as well as excellent charge transfer ability, and thus has aroused rising concern over the past few years [33,34]. Up to now, different kinds of h-BN-based heterostructure photocatalysts, such as, h-BN/g-C_3N_4 [32], h-BN/TiO_2 [35] and h-BN/Ag_3PO_4 [36] have been demonstrated with superior photocatalytic activity. Importantly, recent study of Haastrup's team [37] has theoretically shown that h-BN can remarkably advance the rate of exciton dissociation in monolayer MoS_2, indicating that h-BN have a great potential in photocatalysis. Furthermore, with the size of h-BN shrinking to the quantum dot level, the edge effects and defect centers appear on the boron nitride quantum dots (BNQDs), which endow them with fascinating fluorescence properties and excellent dispersibility [38]. Accordingly, it can be reasonably deduced that the negatively charged oxygen-containing groups on the BNQDs will attract the photo-excited holes, and thus promote the dissociation efficiency of excitons and boost the separation of charges. Similar behavior was previously observed with polyethylene glycol-functionalized graphene quantum dots [39]. However, to the best of our knowledge, the investigation about the roles of BNQDs in photocatalysis is still limited.

Inspired by the above considerations, herein we design and construct a novel metal-free boron nitride quantum dots decorated ultrathin porous g-C_3N_4 (BNQDs/UPCN) heterostructure. The exciton dissociation and charge transfer abilities of BNQDs/UPCN are assessed by steady-state photoluminescence (PL) and time-resolved photoluminescence (TRPL) techniques as well as photoelectrochemical tests. Moreover, the photocatalytic activities of BNQDs/UPCN for the degradation of oxytetracycline hydrochloride (OTC−HCl) and production of H_2O_2 are detailedly investigated. Finally, the reasonable photocatalytic mechanisms over the BNQDs/UPCN photocatalyst are proposed.

2. Experimental section

2.1. Preparation of photocatalysts

2.1.1. Preparation of the ultrathin porous g-C_3N_4

The ultrathin porous g-C_3N_4 (UPCN) was synthesized through a template-free precursor-surface-etching method followed by a thermal polymerization process [40]. Typically, 1.207 g of thiourea was dissolved in 60 mL of deionized water, and then 2.000 g of melamine was uniformly dispersed in the thiourea solution under magnetic stirring for 30 min. The mixture was subsequently transferred into a 100 mL stainless steel autoclave with Teflon liner and heated at 180 °C for 20 h in an oven. The resulting product was gathered through vacuum filtration and respectively washed with deionized water and ethanol for three times, and then dried at 70 °C for 6 h. Finally, the precursor sample was placed in a crucible with a cover and calcined at 520 °C for 3 h with the heating rate of 2.3 °C min^{-1}, followed by cooling to room temperature naturally to yield the UPCN. Besides, bulk g-C_3N_4 (CN) was synthesized via directly annealing 2.000 g of melamine at 520 °C for 3 h with the heating rate of 2.3 °C min^{-1}.

2.1.2. Preparation of the boron nitride quantum dots

The boron nitride quantum dots (BNQDs) were synthesized through a facile hydrothermal procedure [41]. In detail, 0.100 g of boric acid was dissolved in 10 mL of deionized water, and then 0.034 g of melamine was added to the boric acid solution under stirring. After stirring for 20 min, the suspension was transferred into a 25 mL Teflon-lined autoclave and kept at 200 °C for 15 h. After cooling to room temperature, the product was gathered and filtered with ultrafiltration membrane (0.22 μm) to remove large particles. Finally, an aqueous solution containing BNQDs was obtained.

2.1.3. Preparation of the BNQDs/UPCN photocatalysts

The BNQDs/UPCN (BU) photocatalysts were prepared as follows. Firstly, 0.300 g of UPCN was uniformly dispersed in 50 mL of ethanol and sonicated for 60 min. Subsequently, a certain volume of BNQDs solution was added dropwise to the above suspension and stirred for 24 h. Finally, after ethanol was completely vaporized, the BU photocatalysts were collected and dried in a vacuum oven at 70 °C. BU photocatalysts with different BNQDs content designated as BU-X, where "X" denote as the added volume of BNQDs solution (X = 0.5, 1, 3, 5 mL).

2.2. Characterizations

X-ray diffraction (XRD) patterns of the samples were measured on a Bruker D8 Advance instrument with Cu Kα radiation (λ = 0.15418 nm). Fourier transform infrared (FTIR) spectra were collected on a Shimadzu IRAffinity-1 spectrometer using samples embedded in potassium bromide (KBr) pellets. Transmission electron microscopy (TEM) test was carried out on a FEI Tecnai G2 F20 S-TWIN electron microscope at an accelerating voltage of 200 kV. The mapping was collected on a FEI Quanta 250 scanning electron microscopy (SEM) with energy-disperse X-ray spectroscopy (EDS). Atomic force microscopy (AFM) test was performed on a Bruker Multimode 8 instrument. Brunauer-Emmett-Teller (BET) specific surface area were measured by nitrogen adsorption-desorption method using a Micromeritics ASAP 2020 HD88 instrument. X-ray photoelectron spectroscopy (XPS) was collected on a Thermo Escalab 250Xi spectrometer with Al Kα (hν = 1486.6 eV) as the excitation source. Ultraviolet visible diffuse reflectance spectra (UV–vis DRS) were recorded on a Varian Cary 300 spectrophotometer from 350 to 700 nm ($BaSO_4$ as reference material). Photoluminescence (PL) spectra were monitored at room temperature on a PerkinElmer LS-55 fluorescence spectrophotometer with an

excitation wavelength of 320 nm. Time-resolved photoluminescence (TRPL) spectra were measured on a fluorescence spectrophotometer (FLS 980, Edinburgh Instruments).

2.3. Photoelectrochemical measurements

The photoeletrochemical measurements were conducted on a Chenhua CHI 760E electrochemical workstation with a standard three-electrode model. Na_2SO_4 aqueous solution (0.2 M) was used as the electrolyte. A 300 W xenon lamp (CEL-HXF300, Ceaulight) fitted with a 420 nm cutoff filter was utilized to provide light source. The working electrode was prepared as follows: 10 mg of the sample was added into 100 μL of 25% (W/V) PVA solution under ultrasonic treatment to get slurry. Then, the slurry was coated onto a fluorine-doped tinoxide (FTO) glass (1×2 cm^2) which was respectively precleaned by acetone, ethanol and deionized water. Finally, the obtained electrode was dried at 80 °C for 4 h and heated to 120 °C calcined for 1 h. The platinum wire and Ag/AgCl electrode were utilized as the counter electrode and reference electrode, respectively. The transient photocurrent response was measured on an applied voltage of 0 V with the light on or off. The electrochemical impedance spectroscopy (EIS) was collected on an applied voltage of 0 V with an amplitude of 0.005 V over a frequency between 10^{-2} and 10^5 Hz. Moreover, Mott-Schottky curve were also recorded at the frequency of 1000 Hz.

2.4. Photocatalytic degradation evaluation

The photocatalytic activity of all the samples was evaluated by measuring the degradation of OTC−HCl under visible light. A 300 W xenon lamp (CEL-HXF300, Ceaulight) fitted with a 420 nm cutoff filter was utilized to provide light source. Typically, the sample (50 mg) was dispersed in 50 mL of OTC−HCl aqueous solution (10 mg L^{-1}). Prior to irradiation, the suspension was stirred in the darkness for 30 min to reach the adsorption-desorption equilibrium [42–44]. During irradiation, about 3 mL of the reaction solution was taken out at the given irradiation time intervals and centrifuged to remove the powder, and then filtrated with a millipore filter (0.45 μm). The concentration of OTC−HCl was measured by a Shimadzu UV-2700 spectrophotometer at its characteristic absorbance peak (353 nm). The degradation intermediates of OTC−HCl were identified by using a liquid chromatography coupled with tandem mass spectrometry (LC–MS/MS) system. The detailed steps were presented in *Supplementary Material*. Moreover, the total organic carbon (TOC) assays were performed on a Shimadzu TOC-VCPH analyzer. To assess the stability of the sample, after one trial, the powder was gathered via centrifugation and respectively washed with deionized water and ethanol, and dried for the cycle experiment.

For identifying the active species produced in photocatalytic OTC−HCl degradation process of BU-3, the trapping agents, including 4-hydroxy-2,2,6,6-tetramethylpiperidinyloxy (TEMPOL), isopropanol (IPA) and ethylenediaminetetraacetic acid disodium (EDTA-2Na) were utilized to trapping superoxide radicals ($\cdot O_2^-$), hydroxyl radicals ($\cdot OH$) and photo-excited holes (h$^+$), respectively [45]. During the photocatalytic reaction, 5 mM of different quenching agents were dissolved in the OTC−HCl solution. The subsequent operations are the same as the above photocatalytic degradation experiment. Additionally, the electron spin response (ESR) signals of $\cdot O_2^-$ and $\cdot OH$ were monitored on a JEOL JES-FA200 spectrometer under visible light irradiation (λ > 420 nm), where 5,5-dimethyl-1-pyrroline *N*-oxide (DMPO) was used as spin-trapped reagent. The concentration of $\cdot O_2^-$ was estimated by nitroblue tetrazolium (NBT) transformation experiments. The procedure is similar to the aforementioned photocatalytic performance tests with replacing 10 mg L^{-1} OTC−HCl with 0.015 mM NBT. NBT concentration was analyzed by recording the absorbance around 260 nm with a Shimadzu UV-2700 spectrophotometer.

2.5. Photocatalytic hydrogen peroxide production test

The photocatalytic hydrogen peroxide (H_2O_2) production test was conducted by adding 50 mg of photocatalyst in the mixed solution containing 5 mL of isopropanol (IPA) and 45 mL of deionized water (IPA as the electron and proton donor). Before irradiation, the suspension was first ultrasonically dispersed for 10 min, and then stirred in the dark for 60 min with O_2 bubbling to achieve the adsorption-desorption equilibrium. The suspension was subsequently irradiated by a 300 W xenon lamp (CEL-HXF300, Ceaulight) fitted with a 420 nm cutoff filter. At given time intervals, 3 mL of suspension was sampled, centrifuged and filtrated with a millipore filter (0.45 μm) to remove the photocatalyst. The amount of H_2O_2 was determined by iodometry [9]. Typically, 1 mL potassium hydrogen phthalate ($C_8H_5KO_4$) aqueous solution (0.1 M) and 1 mL potassium iodide (KI) aqueous solution (0.4 M) were added to the above solution, and kept for 30 min. Under acidic condition, the H_2O_2 molecules will react with I$^-$ to generate I$_3^-$ (H_2O_2 + 3I$^-$ + 2H$^+$ → I$_3^-$ + 2H_2O). The amount of I$_3^-$ was measured by a Shimadzu UV-2700 spectrophotometer at its characteristic absorbance peak (350 nm), and then the amount of H_2O_2 generated in the reaction was obtained.

3. Results and discussion

3.1. Physicochemical properties

To clarify the crystal structures and chemical features of these samples, XRD and FTIR tests were performed. As displayed in Fig. 1a,
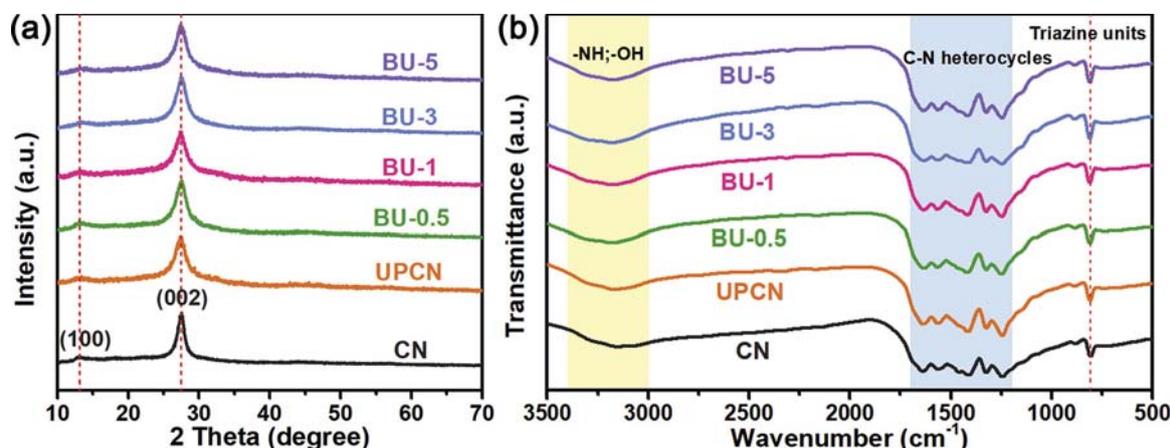
Fig. 1. (a) XRD patterns and (b) FTIR spectra of the CN, UPCN and BU samples.

XRD patterns of all the samples exhibit two similar diffraction peaks which locate at about 13.1° and 27.5°, respectively. The stronger band at 27.5° is indexed to the (002) crystal plane, originating from the stacking reflection of conjugated planes. While the weaker peak loaded at 13.1° is assigned to (100) plane, which is associated with the repetition of nonplanar units [29]. Compared to CN, the peaks of UPCN become broader and weaker, which is ascribed to the porous and ultrathin structure of UPCN. Moreover, after loading of the BNQDs, no significant difference can be seen and no clear boron nitride peaks can be detected. The result suggests that the basic structure of these samples is tetragonal phase g-C_3N_4 and the crystal phase and orientation of g-C_3N_4 have no apparent changes after modification. Meanwhile, it also indicates the low content of BNQDs on the BU samples. Moreover, Fig. 1b presents FTIR spectra of the investigated samples and it is obvious that all the samples show the similar framework. Specifically, the peak situated at 810 cm^{-1} is characteristic signal of triazine units, and the group of peaks between 1200 and 1700 cm^{-1} is ascribed to the typical stretching vibration modes of C–N heterocycles. In addition, the broad peaks ranging from 3000 to 3400 cm^{-1} correspond to -NH and −OH stretching vibrations, indicating that some exposed nitrogen atoms in g-C_3N_4 are partially hydrogenated [32,46]. No distinct peaks of g-C_3N_4 alter, and no boron nitride peaks on BU samples appear, further demonstrating the fundamental structure of g-C_3N_4 and the limited amount of BNQDs on these samples.

TEM images were collected for getting the direct information about morphology and structure of the samples. From Fig. 2a and b, the prepared BNQDs show spherical morphology, and are mainly distributed in 2–4 nm with the average lateral size of about 3 nm, which are in agreement with the previous report [41]. Meanwhile, in comparison with the compact bulk structure of CN in Fig. 2c, the UPCN possesses a clear thinner and porous structure (Fig. 2d). However, the original smooth surface of UPCN becomes rough after loading BNQDs, and some dark dots and pores can be directly observed on the BU-3 sample (Fig. 2e and f). The high-resolution TEM (HRTEM) image of BU-3 further reveals the presence of BNQDs. As exhibited in the insert of Fig. 2f, the dark dot from BU-3 sample has an obvious lattice fringes of 0.21 nm, which is in coincidence with the (100) facet of BN [38,41]. Furthermore, the SEM-EDS elemental mapping of BU-3 (Fig. 2g) also certifies the existence of B, C and N elements, which are uniformly distributed across the sample. These results clearly state the tight hybridization of boron nitride quantum dots with ultrathin porous g-C_3N_4 nanosheets for BU-3 sample.

The thickness of BU-3 was determined by AFM, and the AFM image and the corresponding height distribution profile are presented in Fig. 3a and b, respectively. As shown in Fig. 3b, the average thickness of the nanosheet is about 2.6 nm, demonstrating the ultrathin nanosheet structure of BU-3, which embodies about 7 atomic layers of g-C_3N_4. Meanwhile, the extra 0.7 nm height can be attributed to the different layer of g-C_3N_4 according to the Fig. 2e [40]. Besides, Fig. 3c displays the nitrogen adsorption-desorption isotherms and the pore size distribution curves for CN, UPCN and BU-3. According to the IUPAC classification, the CN holds a type II isotherm while the UPCN and BU-3 possess a type IV isotherm, indicating the characteristics of nonporous and mesoporous materials, respectively [27,40,47]. The pore size distribution curves (insert of Fig. 3c) also prove these results. Moreover, the BET specific surface areas of CN, UPCN and BU-3 are measured to be 6.2, 23.2 and 24.5 $m^2 g^{-1}$, which increase in turn and will provide more reaction active sites for photocatalysis. These results further
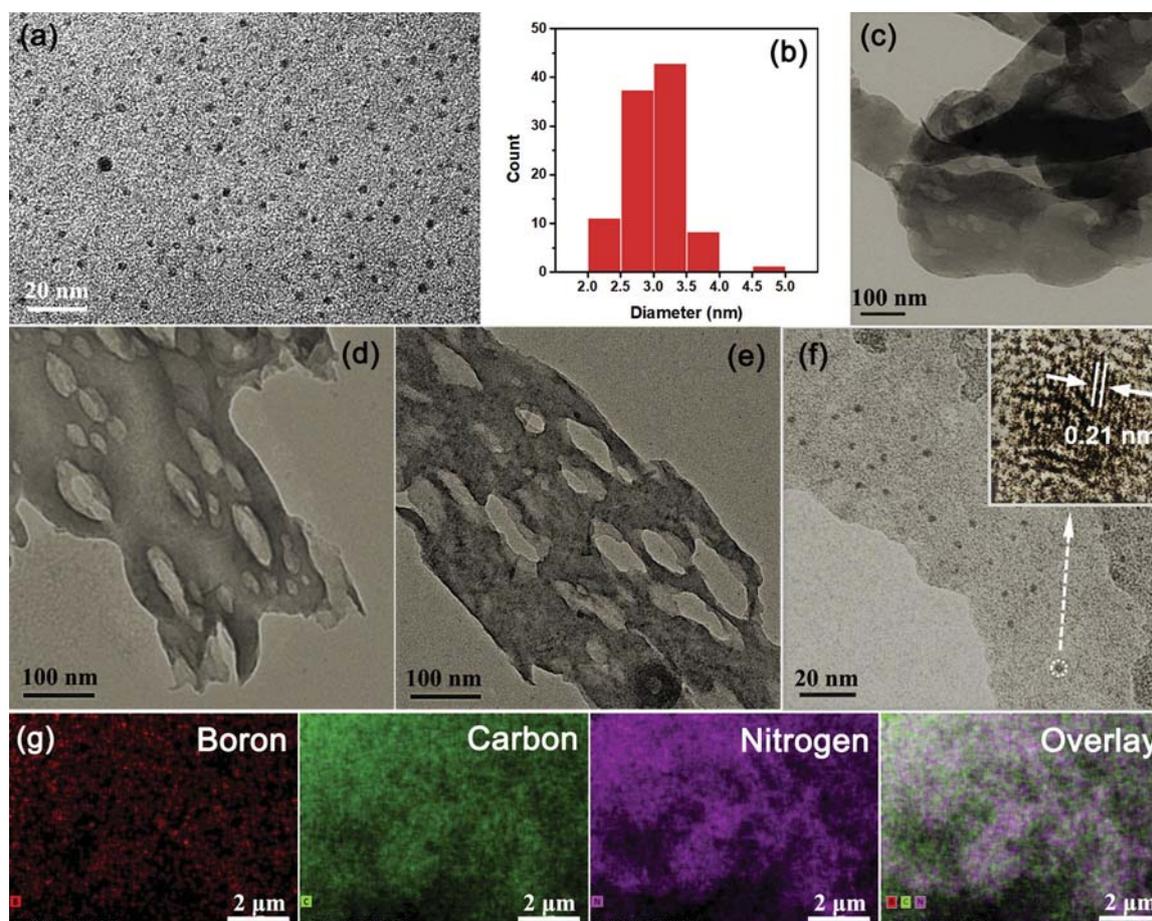
Fig. 2. (a) TEM image of BNQDs and (b) corresponding size distribution of BNQDs; TEM images of (c) CN, (d) UPCN and (e and f) BU-3 (insert, HRETM); (g) SEM-EDS elemental mapping for BU-3.
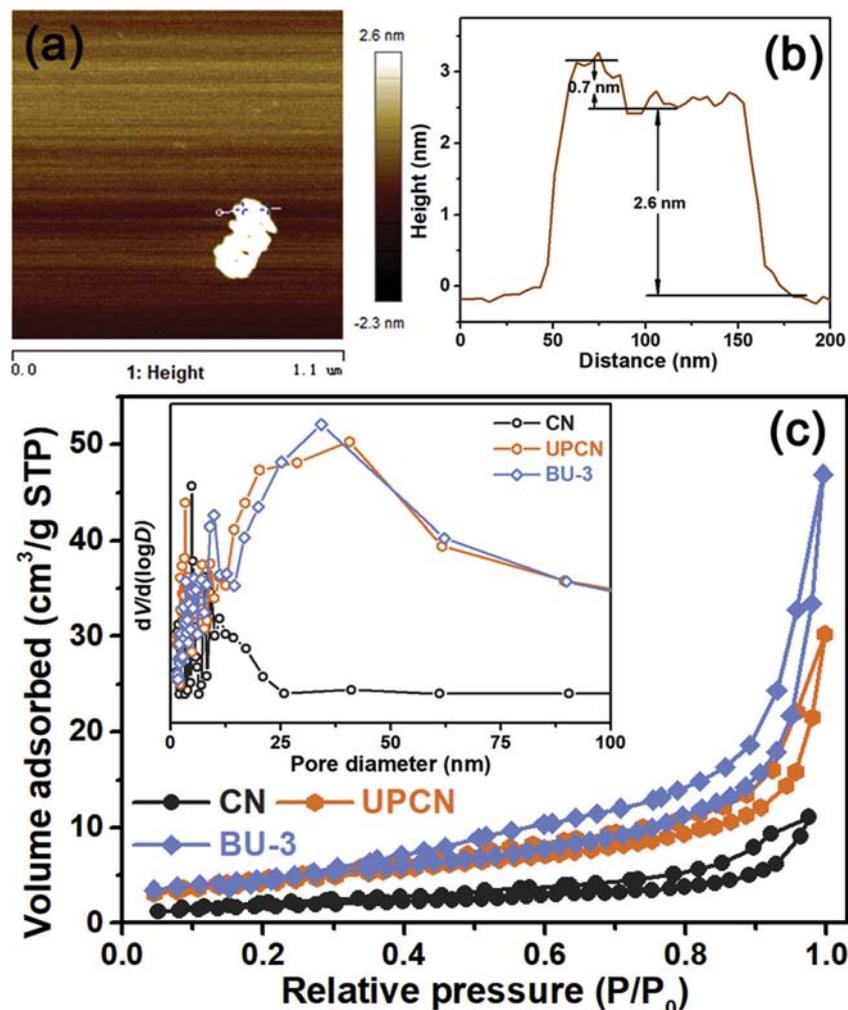
Fig. 3. (a) AFM image and (b) the height distribution profile of BU-3; (c) Nitrogen adsorption-desorption isotherms and the pore size distribution curves (insert) for CN, UPCN and BU-3.

highlight the ultrathin and porous nanostructures of BU-3 as well as the successful introduction of BNQDs.

XPS technique was utilized to analyze the surface chemical states of the samples. As exhibited in Fig. 4a, three elements of C, N and O are detected in the UPCN while four elements of B, C, N and O are found in the BU-3. The signal of O element is attributed to the chemisorbed oxygen. To get detailed chemical states information, the high-resolution XPS spectra of C 1 s, N 1 s and B 1 s were recorded. For C 1 s, as illustrated in Fig. 4b, three peaks at the binding energies of 284.8, 286.0 and 288.4 eV can be seen. The binding energy at 284.8 eV is related to the adventitious carbon contamination during the measurement [40]. The binding energies at 286.0 and 288.4 eV can be ascribed to sp^3-coordinated carbon (C–N) and sp^2-hybridized carbon (N–C=N), respectively [48]. Meanwhile, the N 1 s spectrum in Fig. 4c can be divided into three peaks at 398.8, 399.5 and 401.1 eV, which are assigned to the sp^2-bonded nitrogen in C=N–C, the N-(C)₃ groups of skeleton, and the terminal C–N-H amino functions, respectively [29]. Compared with UPCN, the new binding energies at 398.2 and 399.2 eV of BU-3 are assigned to N–B and C–N–B bonds [49]. Additionally, the B 1 s spectrum of BU-3 can be deconvoluted into two peaks as shown in Fig. 4d. The stronger peak at 190.6 eV is a characteristic signal for the B–N stretching vibration, while the weaker peak appearing at 191.9 eV is referred to B–O bonds, indicating the existence of oxygen-containing groups on the surface of BNQDs [38,41]. Therefore, combining with the mentioned above results, it can be concluded that the successful preparation of BNQDs/UPCN photocatalysts.

Fig. 5a depicts UV–vis DRS of the as-prepared samples. The CN exhibits almost no light absorption above 500 nm, whereas the UPCN presents elevated visible light absorption because the porous structure can promote the multiple reflection of incident light [40]. Compared with the UPCN, the absorption edge of BU samples shows somewhat blue-shift due to the existence of BNQDs, but they still hold distinct visible light absorption. The band gap energy of CN and UPCN were evaluated through the transformational Taus plots acquired from the Kubellka-Munk function. As seen from the Fig. 5b, the band gap energy is determined to be 2.56 and 2.54 eV for CN and UPCN, respectively. The UPCN possessed a narrower band gap than CN, which could be ascribed to a small amount of N self-doping [27,40]. The valence band (VB) XPS technique was used to obtain the information of VB. From Fig. 5c, the VB potential of CN and UPCN are estimated to be 1.62 and 1.59 V, respectively. Therefore, the conduction band (CB) potential of CN and UPCN are calculated to be –0.94 and –0.95 V from the formula $E_{CB} = E_{VB} - E_g$ (E_g, E_{CB} and E_{VB} indicate the band gap energy, CB potential and VB potential) [50,51], and the detailed band structure diagram is illustrated in Fig. 5d.

3.2. Exciton dissociation and charge transfer abilities

In organic semiconductors, photo-excited electrons and holes are easily bound together to generate excitons [19,20]. However, effective exciton dissociation is necessary for photocatalysis. Herein, photoluminescence tests were conducted to study the involved excitonic
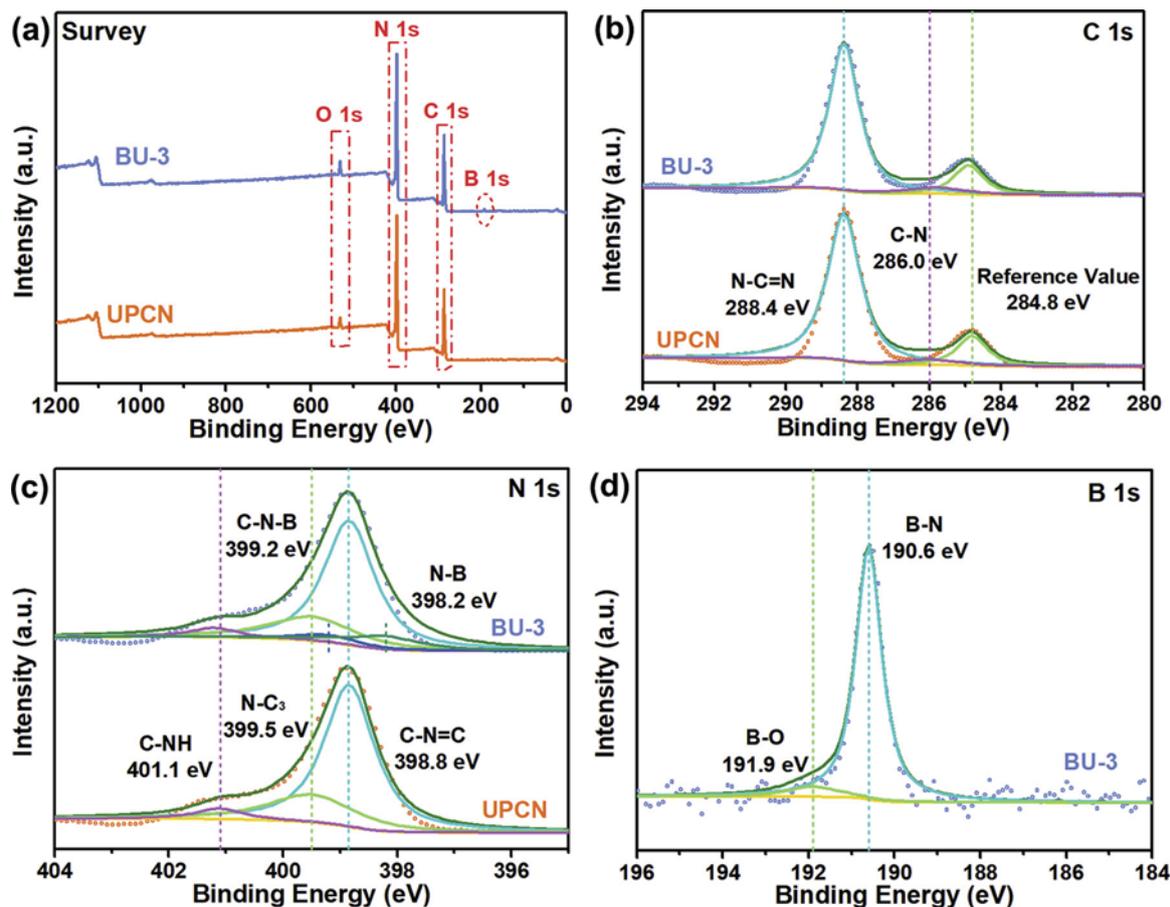
Fig. 4. XPS spectra of UPCN and BU-3 samples: (a) total survey, (b) C 1 s, (c) N 1 s and (d) B 1 s.

processes [17,52]. Steady-state photoluminescence (PL) technique is an important method to investigate the property of radiative recombination process. As exhibited in Fig. 6a, CN possesses a strongest emission peak at the wavelength of 454 nm owing to the radiative recombination effect of self-trapped excitons. In contrast to CN, UPCN and BU samples present apparently reduced emission peak intensity, in which BU-3 shows a lowest emission peak at 465 nm. The dramatically decreased emission peak intensity indicates the distinctly reduced population of excitons because photoluminescence phenomenon stems from the recombination of singlet excitons [17]. It can be inferred that BU-3 photocatalyst can profit from ultrathin porous nanostructures and BNQDs, elevating the dissociation efficiency of excitons and inhibiting the recombination of charge carriers.

To get the average radiative lifetime of the recombining charge carriers, the time-resolved photoluminescence (TRPL) measurements were performed on CN, UPCN and BU-3 at their corresponding emission peak, as displayed in Fig. 6b. The fluorescence decay curves of them were fitted using the double-exponential function [53]:

$$R(t) = B_1 \exp(-t/\tau_1) + B_2 \exp(-t/\tau_2) \tag{1}$$

Where B_1 and B_2 are the pre-exponential factor, and τ_1 and τ_2 are the radiative lifetime. Obviously, both of the two radiative lifetimes of BU-3 photocatalyst are diminished. The average radiative lifetime (τ_{ave}) was further calculated according to the following equation [53]:

$$\tau_{ave} = \frac{B_1\tau_1^2 + B_2\tau_2^2}{B_1\tau_1 + B_2\tau_2} \tag{2}$$

The τ_{ave} for CN is 9.05 ns, while for the UPCN and BU-3 are 8.33 and 7.09 ns, respectively. The remarkably shortened singlet exciton lifetime evidently demonstrates promoted exciton dissociation in the BU-3

photocatalyst, which can be ascribed to the ultrathin porous nanostructures of g-C$_3$N$_4$ as well as the presence of BNQDs [20]. Thus, the declination of photoluminescence intensity together with the shortened radiative lifetime certifies the increased exciton dissociation on BU-3 photocatalyst.

The interfacial charge transfer behaviors were investigated by transient photocurrent response curves and electrochemical impedance spectroscopy (EIS) [54,55]. Fig. 7a depicts the photocurrent-time signals for CN, UPCN and BU-3 under several on-off cycles of illumination ($\lambda > 420$ nm). CN shows the lowest current density because of the rapid recombination of photo-generated electron-hole pairs. Meanwhile, the UPCN possesses the higher current density compared with that of CN, whereas the highest current density is presented in the BU-3. The enhanced photocurrent density validates that not only ultrathin porous nanostructures can endow g-C$_3$N$_4$ with highly efficient electron transfer, but also the BNQDs are in favor of its interfacial charge transfer. Additionally, EIS analysis was carried out to get further information on the charge transfer process [56]. Fig. 7b displays the EIS Nyquist plots of the three samples, the radius of arc is generally connected with the resistance at the electrode-electrolyte interface, and a shorter arc radius represents a lower charge transfer resistance [57,58]. The arc radius of CN, UPCN and BU-3 decrease in turn, wherein the BU-3 owns the smallest charge transfer resistance, implying a higher interfacial charge transfer rate. Moreover, as shown by the bode phase spectra in Fig. 7c, the frequency peak of BU-3 shifts mildly to a lower frequency compared with CN and UPCN, indicating a more rapid electron transfer process [40,59].

Furthermore, Mott-Schottky tests were conducted to determine the charge carrier density on the samples, and the results are exhibited in Fig. 7d. The positive slopes of CN, UPCN and BU-3 indicate that they
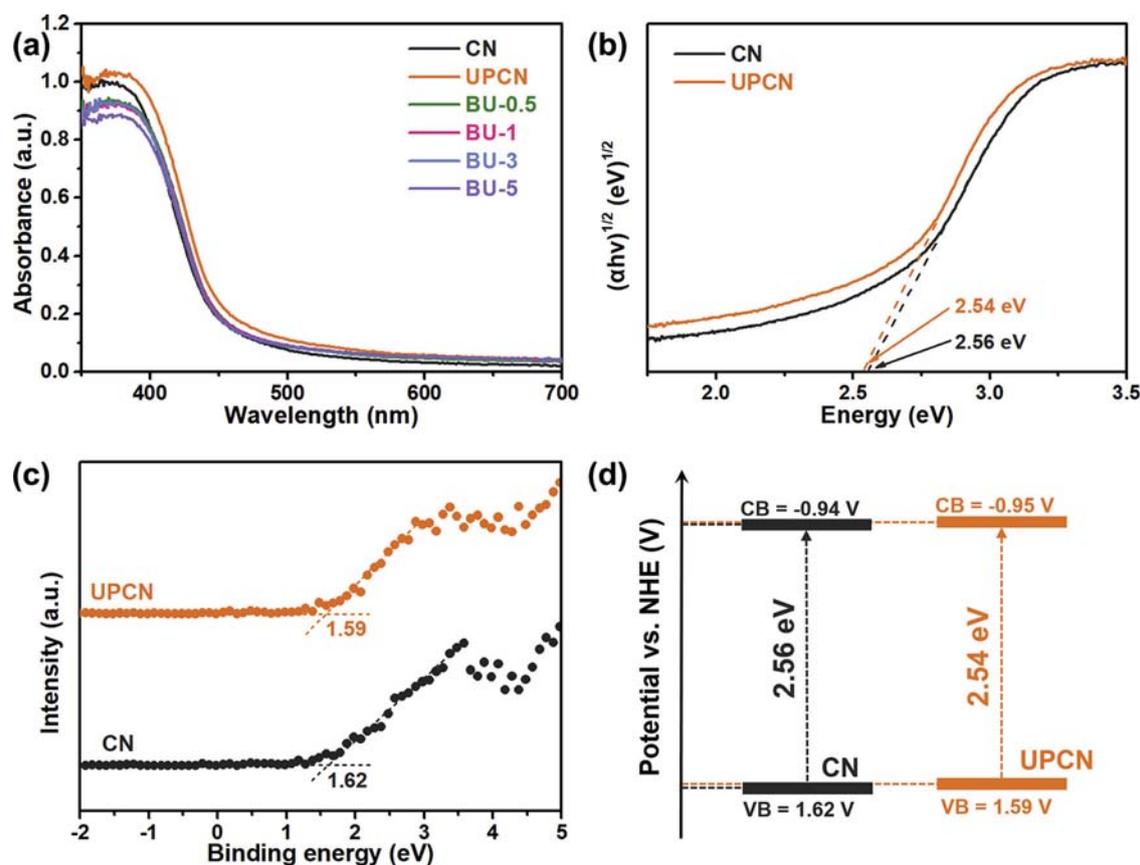
Fig. 5. (a) UV–vis DRS for the all samples; (b) Band gap energy plots, (c) VB XPS spectra and (d) band structure diagrams for CN and UPCN.
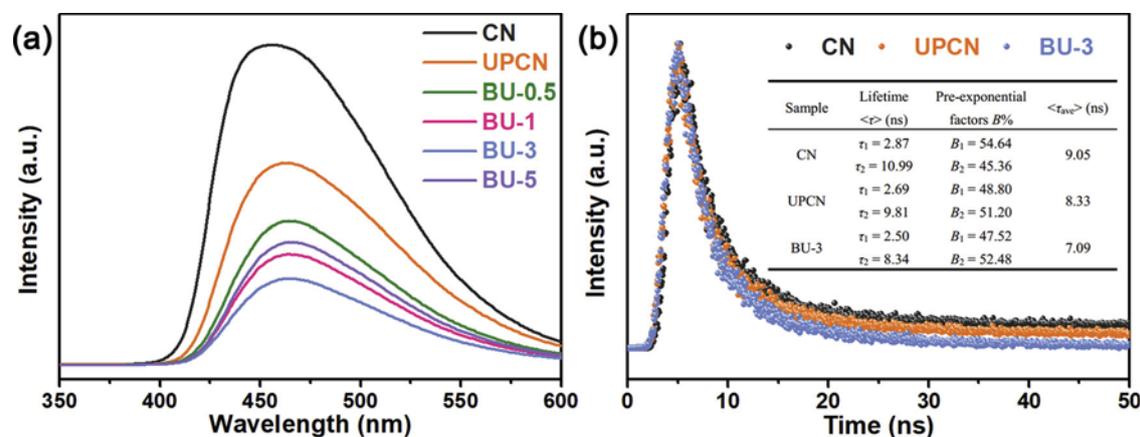
Fig. 6. (a) Steady-state photoluminescence spectra and (b) time-resolved photoluminescence decay spectra of the as-prepared samples.

are all n-type semiconductors with electron conduction. Therefore, the charge carrier density (N_D) of the samples can be quantified from the slop of Mott-Schottky curves by the following formula [60]:

$$N_D = \frac{2}{q\varepsilon\varepsilon_0}\frac{dE}{d(1/C^2)} = \frac{2}{q\varepsilon\varepsilon_0}\frac{1}{\text{slope}}$$

(3)

Where q is the electron charge (1.602×10^{-19} C), ε and ε_0 represent the dielectric constant of the sample (5.25 for g-C$_3$N$_4$) and the permittivity of vacuum (8.85×10^{-14} F cm^{-2}) respectively, and the slope refers to the liner part in the Mott-Schottky curve. According to the formula, the N_D of BU-3 is calculated to be 1.65×10^{24} cm^{-3}, which is much greater than that of UPCN (1.22×10^{24} cm^{-3}) and CN (1.10×10^{24} cm^{-3}). The significantly increased electron concentration in the BU-3 is indicative of the higher dissociation of excitons. This

enhanced dissociation lowers the recombination of charge carriers, thereby elevating the electron concentration, which is in accordance with the above results.

3.3. Photocatalytic activities and mechanisms

The photocatalytic activities of BNQDs/UPCN (BU) nanocomposites were tested through the degradation of oxytetracycline hydrochloride (OTC−HCl) under visible light irradiation ($\lambda > 420$ nm). Fig. S1 demonstrates that the adsorption ratio in the darkness of all the samples are less than 3% following the adsorption-desorption equilibrium [61–64]. Fig. 8a depicts the change in OTC−HCl concentration (C_t/C_0) with irradiation time over the CN, UPCN and BU photocatalysts under visible light irradiation. The C_0 represents the concentration of
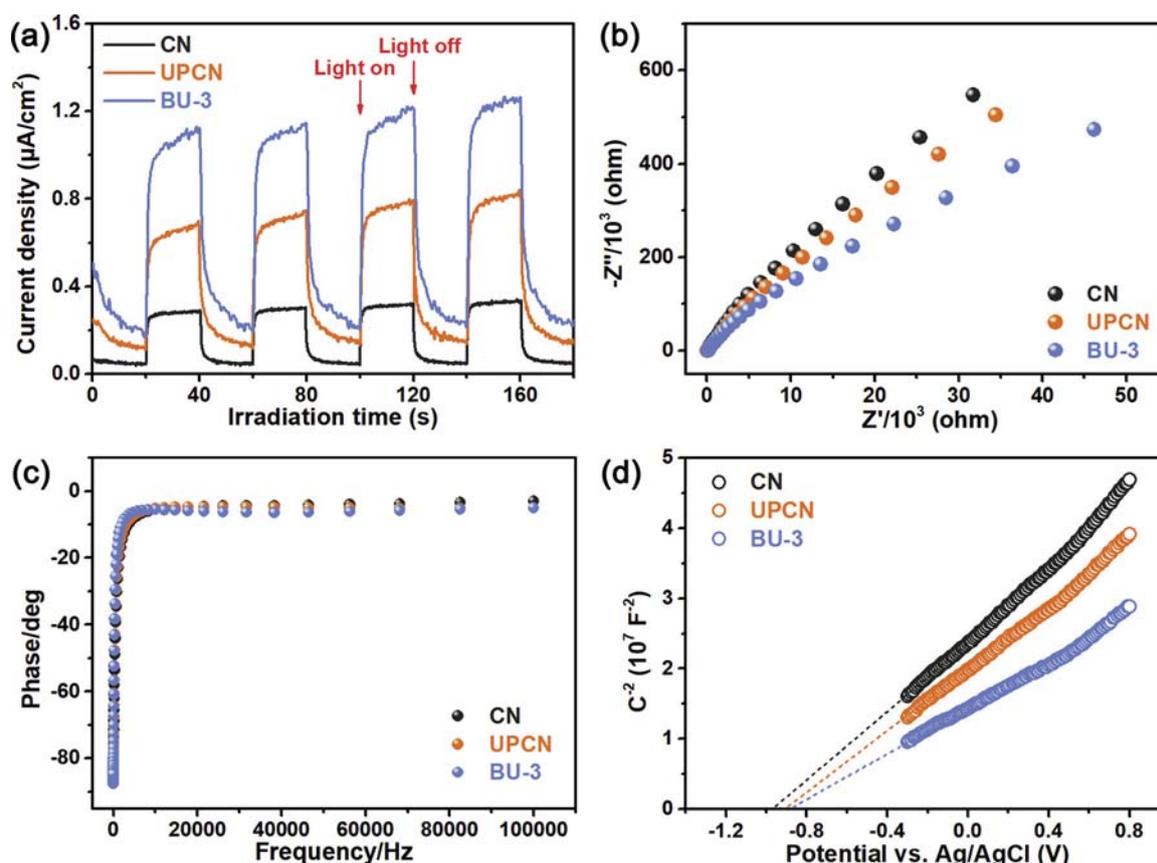
Fig. 7. (a) Transient photocurrent response curves, (b) Nyquist plots of electrochemical impedance spectroscopy, (c) Bode phase spectra and (d) Mott-Schottky plots of CN, UPCN and BU-3.

OTC−HCl after reaching adsorption-desorption equilibrium, and the C_t refers to the concentration of OTC−HCl after time t of photocatalytic reaction. Meanwhile, the photocatalytic degradation efficiency (DE, %) was calculated by the following equation and shown in Fig. 8b:

$$DE(\%) = (1 - C_t/C_0) \times 100\% \tag{4}$$

Obviously, the natural photolysis of OTC−HCl in the absence of photocatalyst is negligible, demonstrating the high stability of OTC−HCl under visible light. CN and UPCN possess degradation efficiencies of approximately 31% and 52% after 60 min of photocatalytic reaction, respectively. The degradation efficiencies on the BU samples are all remarkably higher than that of CN and UPCN. With an increasing proportion of BNQDs, the photocatalytic degradation activity of BU exhibits an increasing trend. The highest photocatalytic degradation efficiency of OTC−HCl (82%) is presented in the BU-3 sample. Fig. S2 displays the time-dependent UV–vis spectrum of OTC−HCl on the BU-3, it is apparent that the intensity of characteristic absorption peak at 353 nm declines with the time prolongs. Nevertheless, the photocatalytic performance of BU decreases when the BNQDs exceed the optimal proportion, indicating that the presence of more BNQDs in this nanocomposite does not necessarily obtain the best photocatalytic performance because excessive BNQDs will depress the light harvesting ability and mask the active spots of g-C$_3$N$_4$.

The apparent rate constant (k) for the degradation of OTC−HCl was further assessed by the following equation:

$$k = \frac{\ln(C_0/C_t)}{t} \tag{5}$$

As displayed in Fig. 8c, the plots of $\ln(C_0/C_t)$ versus t are found to be a linear relationship, clarifying that the reaction of OTC−HCl photocatalytic degradation is in coincidence with the pseudo-first-order model. From the kinetic curves, the k value conforms the order: BU-3

(0.0309 min^{-1}) > BU-1 (0.0273 min^{-1}) > BU-5 (0.0239 min^{-1}) > BU-0.5 (0.0206 min^{-1}) > UPCN (0.0144 min^{-1}) > CN (0.0072 min^{-1}). The BU-3 photocatalyst presents the highest apparent rate constant of 0.0309 min^{-1}, which is about 4.3 and 2.1 times than that of CN and UPCN, respectively. The enhanced photocatalytic performance is originated from the ultrathin porous nanostructures as well as the introduction of BNQDs, which can promote the dissociation of excitons and accelerate the transfer of charges.

In order to understand the degradation process of OTC−HCl over BU-3 photocatalyst deeply, the LC−MS/MS analysis was carried out. The MS spectra and possible intermediates products (after 60 min of degradation) is presented in the Fig. S3 and Table S1, respectively. On the basis of the LC−MS/MS results and previous reports, the possible degradation pathways of OTC−HCl are proposed and illustrated in Scheme 1. First OTC−HCl is transformed to OTC through hydrolysis reaction. Then the OTC is decomposed to OTC 1 via the loss of one *N*-methyl, and the OTC 1 is degraded to OTC 2 via loss of another *N*-methyl [65]. Subsequently, OTC 2 is decomposed to produce OTC 3 via the dehydration reaction, which further results to the generation of OTC 4 through the deamidation reaction [66]. OTC 2 can also be transformed to OTC 5 via the loss of a hydroxyl group and an amino group [67]. With the loss of formyl groups, carbonyl group, hydroxyl group and methyl, the OTC 5 is decomposed to OTC 6. And the OTC 7 is arisen from OTC 6 through the loss of amino groups and oxidative dihydroxylation [68]. Meanwhile, OTC can be transformed to OTC 8 by hydroxylation process. Moreover, the TOC removal efficiency was tested to evaluate the mineralization ability of BU-3 photocatalyst. As shown in Fig. S4, the removal efficiency of TOC in OTC−HCl aqueous solution is 18% within 60 min of visible light irradiation. These results further demonstrate that the BU-3 photocatalyst has efficient photocatalytic degradation activity for OTC−HCl.
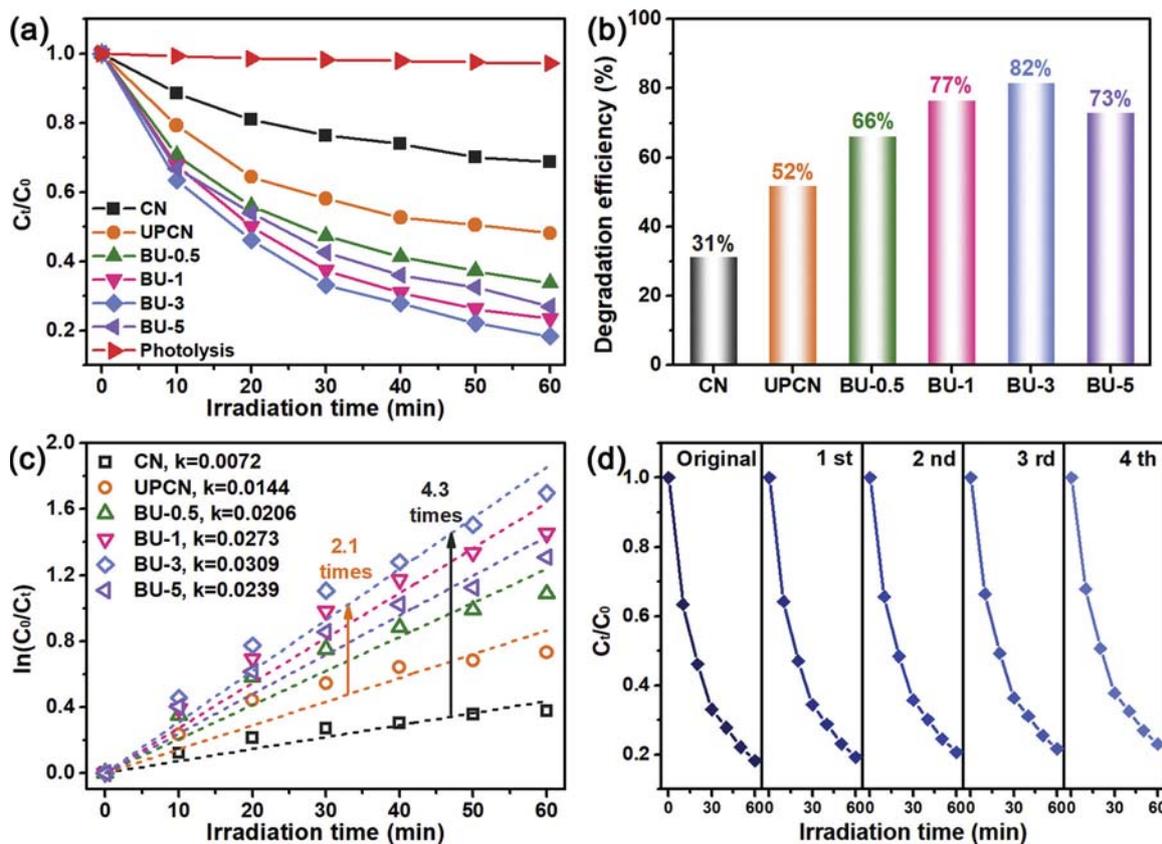
Fig. 8. (a) Photocatalytic degradation curves and (b) degradation efficiencies of OTC−HCl under visible light irradiation ($\lambda > 420$ nm) for different samples; (c) Pseudo first-order kinetic fitting curves and the corresponding apparent rate constants (*k*); (d) Cycling runs for the OTC−HCl photocatalytic degradation over BU-3 photocatalyst.

Besides, the recyclability and physicochemical stability of the BU-3 in the OTC−HCl photocatalytic degradation was explored. The cyclic experiments were performed and the results are shown in Fig. 8d. Clearly, a quite high OTC−HCl degradation efficiency of 77% is still achieved on BU-3 photocatalyst after four cycles of repeated use. Moreover, the physicochemical properties of the BU-3 sample after repeated use of four times were characterized by the XRD (Fig. S5c) techniques, and no apparent changes are observed in them. These

results verify the significant recyclability and physicochemical stability of BU-3 photocatalyst in the photocatalytic degradation of OTC−HCl.

To investigate the contribution of the various oxidative species generated in the BU-3 photocatalytic system for the degradation of OTC−HCl, active species trapping tests were executed through adding quenchers. Herein, TEMPOL, IPA and EDTA-2Na were employed as the quenchers of $\cdot O_2^-$, $\cdot$OH and h$^+$, respectively [45]. Fig. 9a and b depicts the photocatalytic degradation curves and degradation efficiencies of
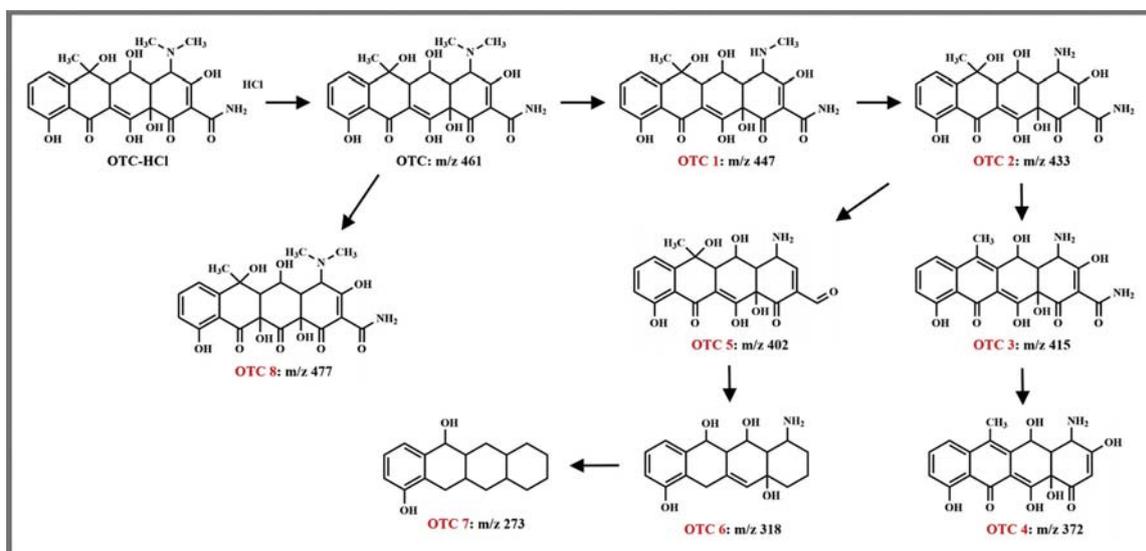
Scheme 1. Proposed photocatalytic degradation pathways of OTC−HCl.
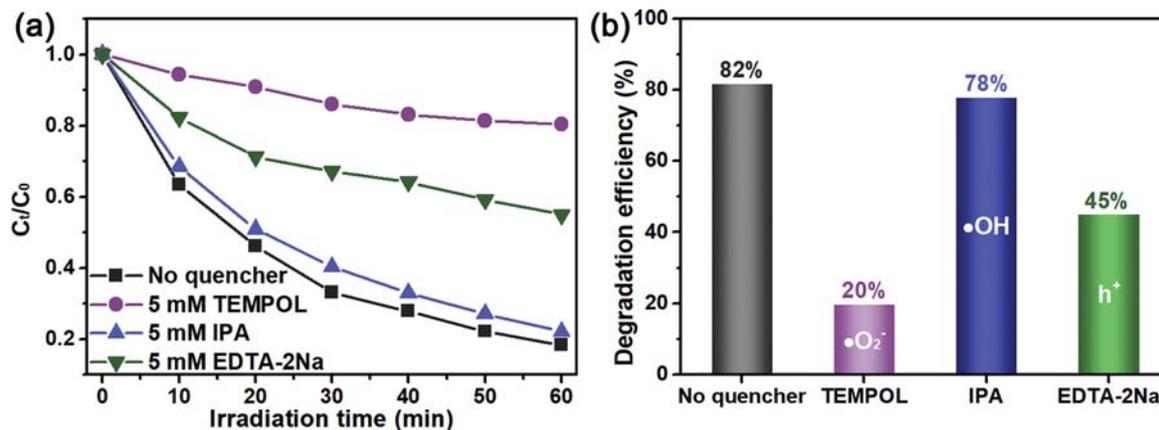
Fig. 9. (a) Photocatalytic degradation curves and (b) degradation efficiencies of OTC−HCl under visible light irradiation ($\lambda > 420\,nm$) over BU-3 photocatalyst with different quenchers.

OTC−HCl over BU-3 photocatalyst under visible light irradiation in presence of this three quenchers. When 5 mM TEMPOL and 5 mM EDTA-2Na are added into the photocatalytic system, the degradation efficiency of OTC−HCl remarkably decrease from 82% to 20% and to 45%, respectively. However, the presence of 5 mM IPA only reduces the degradation efficiency of OTC−HCl from 82% to 78%. These results reveal that the $\cdot O_2^-$ and h^+ are the major reactive species in photocatalytic degradation of OTC−HCl for BU-3 photocatalyst, while the $\cdot OH$ contribute a little to the degradation process.

The NBT transformation experiments were conducted for determine the amount of $\cdot O_2^-$ produced in the photocatalytic process. As exhibited in Fig. 10a-c, for CN, UPCN and BU-3, the intensity of characteristic absorption peak at 260 nm of NBT all significantly decline after photocatalytic reaction, indicating that $\cdot O_2^-$ is the major reactive species for the three samples during photocatalytic process. It can be obviously observed from the Fig. 10d and e that the BU-3 possesses the optimal degradation efficiency for NBT and its apparent rate constant (k) is about 2.9 and 1.7 times than that of CN and UPCN, which is owing to the increased production of $\cdot O_2^-$. Therefore, in the basis of the reaction relationship between $\cdot O_2^-$ and NBT (molar ratio is 4:1), the average $\cdot O_2^-$ production rates of CN, UPCN and BU-3 are estimated to be 0.11, 0.16 and 0.25 $\mu mol\,L^{-1}\,min^{-1}$, respectively (Fig. 10f). This

result further confirms the enhanced photocatalytic performance of BU-3 in $\cdot O_2^-$ formation.

Meanwhile, to further assess their photocatalytic activities, H_2O_2 production ability under visible light irradiation over the BU hybrids were investigated. As displayed in Fig. 11a, the amount of H_2O_2 produced on the BU-3 is 72.30 $\mu mol\,L^{-1}$ in 60 min, which is higher than that of CN (22.77 $\mu mol\,L^{-1}$) and UPCN (36.13 $\mu mol\,L^{-1}$). Fig. S6 shows the UV–vis absorption spectrum changes of H_2O_2 generation of BU-3. Obviously, the absorbance at 350 nm gradually increases with the prolongation of reaction time. This result indicates that the ultrathin and porous structure as well as the implantation of BNQDs promote the photocatalytic production of H_2O_2 on g-C_3N_4. Moreover, some control experiments were conducted for comparison. As shown in Fig. 11b, the H_2O_2 can be hardly detected without the visible light irradiation or photocatalyst, suggesting that the photocatalysis plays a decisive role in the H_2O_2 production process. Furthermore, the H_2O_2 also cannot be produced when oxygen is replaced by nitrogen gas, and the amount of H_2O_2 reduces significantly in the absence of IPA, demonstrating that the H_2O_2 is derived from the two-electron reduction of oxygen rather than the oxidation of water by the photo-generated holes.

Besides, the generation of reactive oxygen species on the samples was monitored via a DMPO spin-trapping ESR technique. As shown in
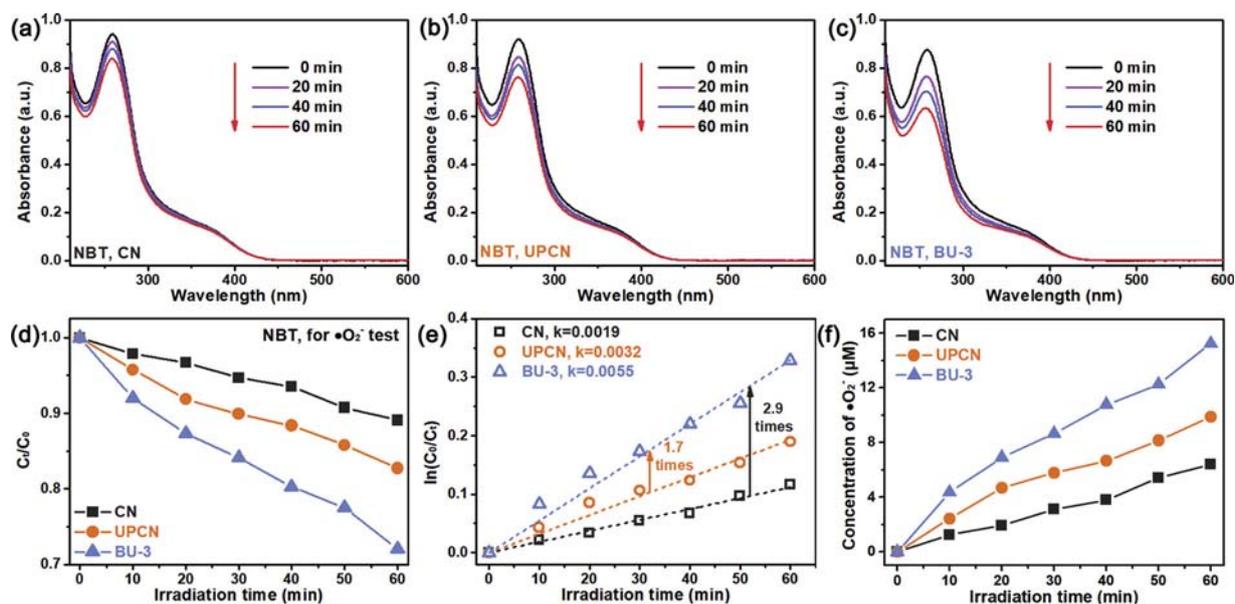
Fig. 10. Absorption spectra of NBT solution over (a) CN, (b) UPCN and (c) BU-3 under visible light irradiation ($\lambda > 420\,nm$); (d) Time-dependent degradation curves of NBT over the samples and (e) the corresponding pseudo first-order kinetic fitting curves; (f) Time-dependent concentration plots of $\cdot O_2^-$.
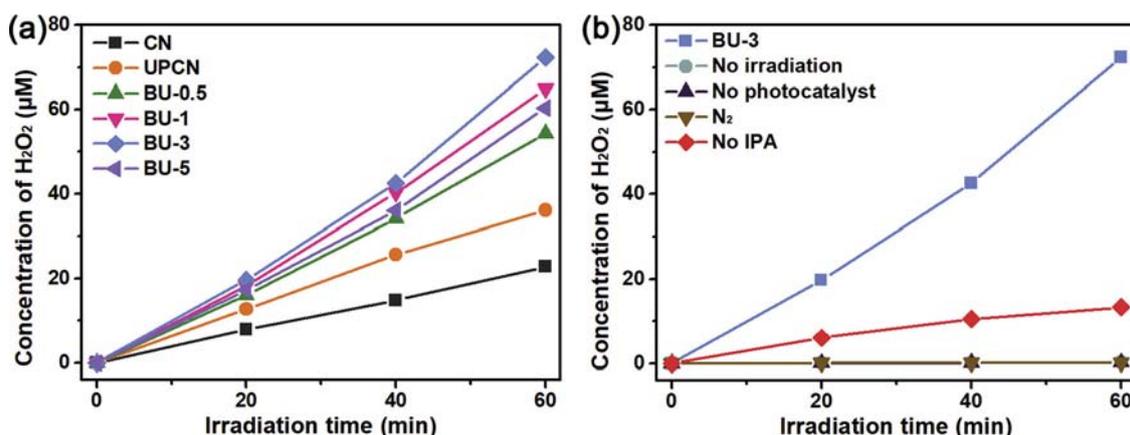
Fig. 11. (a) Photocatalytic production of H_2O_2 under visible light irradiation ($\lambda > 420$ nm) over different samples; (b) Comparison of the photocatalytic production of H_2O_2 under different conditions for BU-3.

Fig. 12a and b, no ESR signals appear in the dark for CN, UPCN and BU-3 samples. Upon visible light irradiation, a characteristic quartet signal of DMPO-•O_2^- adduct with an intensity ratio of 1:1:1:1 is detected in all them (Fig. 12a). Importantly, the intensity of DMPO-•O_2^- adduct signal for BU-3 photocatalyst is stronger than that of CN and UPCN, which is ascribed to the significantly increased concentration of free electrons, promoting the generation of ˙O_2^-. Meanwhile, a four-line ESR signal of DMPO-•OH adduct with an intensity ratio of 1:2:2:1 is also detected in all of the samples (Fig. 12b), which variation trend is consistent with ˙O_2^-. However, the VB potential of CN and UPCN are tested to be 1.62 and 1.59 V, while the standard redox potential of OH^-/˙OH or H_2O/˙OH are 1.99 and 2.37 V [69]. The more negative VB potential of these samples than the standard redox potential of OH^-/˙OH or H_2O/˙OH indicates that the samples cannot oxidize OH^- or H_2O to ˙OH under visible light thermodynamically [70,71]. Therefore, ˙OH may be originated from the reduction of ˙O_2^- (˙O_2^- + e^- + $2H^+$ → H_2O_2, H_2O_2 + e^- → OH^- + ˙OH), further demonstrating the photocatalytic production of H_2O_2.

Based on the above results and analyses, possible photocatalytic mechanisms over the BNQDs/UPCN nanocomposite is proposed in Scheme 2. Under visible light irradiation ($\lambda > 420$ nm), the UPCN is excited to generate electron-hole pairs, which are easily bound together to form excitons because of the Coulomb interactions. However, owing to the ultrathin nanostructure, more excitons can diffuse to the surface and can be turned into dissociated. Meanwhile, the BNQDs can efficiently attract and thus accelerate the transfer of photo-excited holes in UPCN due to the presence of negatively charged edge functional groups, significantly facilitating excitons dissociate into hot carriers and

depressing recombination of charges. Moreover, the ultrathin porous nanostructure is in favor of the transfer of hot electrons, thereby remarkably restraining the recombination of photo-generated carriers. With respect to OTC−HCl degradation, the hot electrons are easy to react with molecular oxygen to form ˙O_2^- because the CB position of UPCN (-0.95 V vs NHE) is negative than the redox potential of O_2/˙O_2^- (-0.33 V vs NHE). And the ˙O_2^- can further react with H^+ to form ˙OH. Finally, the produced active species (˙O_2^-, ˙OH and h^+) on the surface of BNQDs/UPCN photocatalyst react with the OTC−HCl molecule, resulting in its degradation. The reaction process can be described as follows:

$$BNQDs/ UPCN+ hv \rightarrow BNQDs/UPCN\ (e^- + h^+) \tag{6}$$

$$e^- + O_2 \rightarrow \bullet O_2^- \tag{7}$$

$$\bullet O_2^- + e^- + 2H^+ \rightarrow H_2O_2 \tag{8}$$

$$H_2O_2 + e^- \rightarrow OH^- + \bullet OH \tag{9}$$

$$(\bullet O_2^-,\ h^+,\ \bullet OH) + OTCHCl \rightarrow products \tag{10}$$
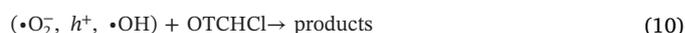
While for the photocatalytic production of H_2O_2, it can be generated through a two-electron reduction of O_2 as the CB level of UPCN (-0.95 V vs NHE) is more negative than the redox potential of O_2/H_2O_2 (0.68 V vs NHE), and the reaction process is list as follows:

$$CH_3CHOHCH_3 + 2h^+ \rightarrow CH_3COCH_3 + 2H^+ \tag{11}$$

$$O_2 + 2H^+ + 2e^- \rightarrow H_2O_2 \tag{12}$$
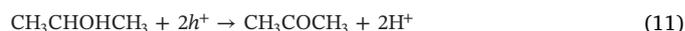
Therefore, the improved photocatalytic performance of BNQDs/
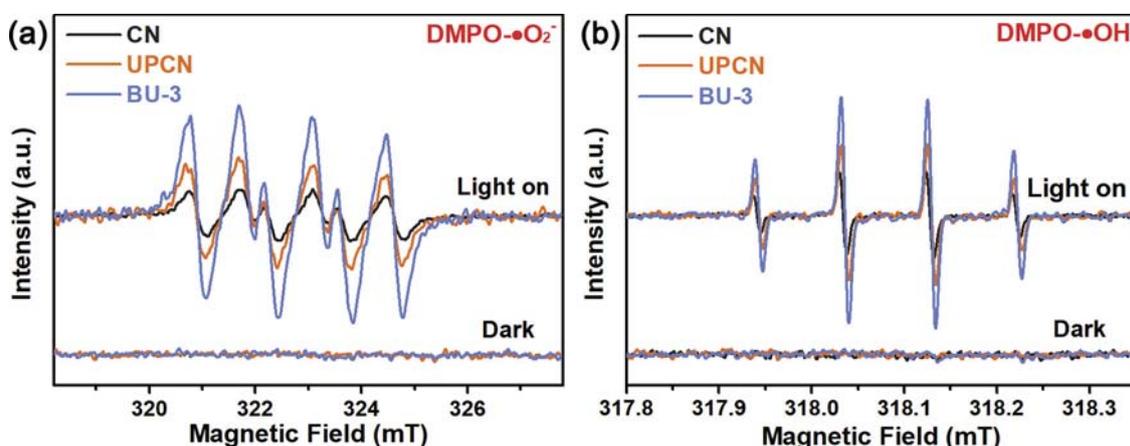
Fig. 12. ESR spectra of (a) DMPO-˙O_2^- adduct and (b) DMPO-•OH adduct for CN, UPCN and BU-3 under visible light irradiation ($\lambda > 420$ nm).
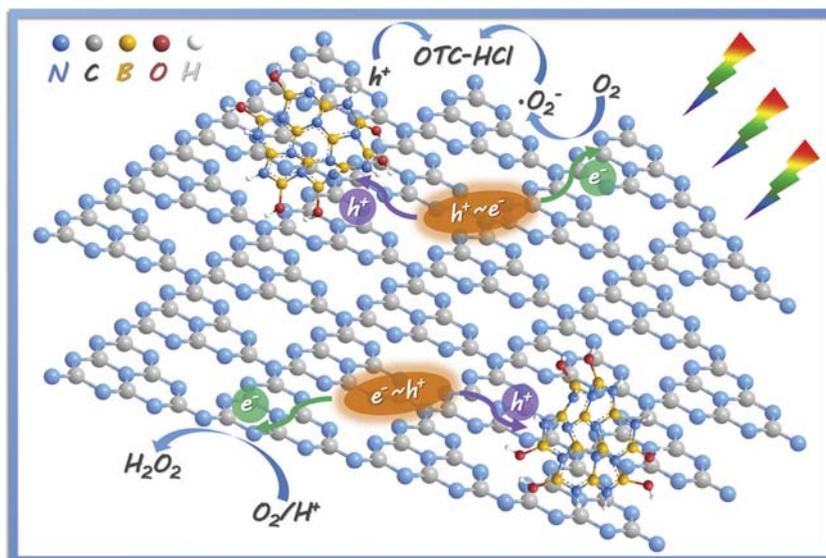
Scheme 2. Proposed photocatalytic mechanisms in BNQDs/UPCN heterostructure.

UPCN heterostructure can be attributed to the enhanced dissociation of excitons and accelerated transfer of charges, which notably promote the separation of photo-excited electron-hole pairs and advance the activation of molecular oxygen.

4. Conclusions

In summary, a metal-free BNQDs/UPCN (BU) heterostructured photocatalyst was successfully developed via a facile method. PL and TRPL analyses as well as photoelectrochemical test results demonstrated the intensified exciton dissociation and charge transfer. Owing to the accelerated separation of photo-excited electron-hole pairs, which can significantly elevate the concentration of hot electrons and advance the activation of molecular oxygen, the BU photocatalysts presented superior photocatalytic activities toward OTC−HCl degradation and H_2O_2 production under visible light irradiation ($\lambda > 420$ nm). This study sheds new light on how rational hybridization of g-C_3N_4 with BNQDs can lead to excellent photocatalytic activity. Moreover, it also puts forward a highly efficient and environment friendly strategy for environmental remediation and energy conversion.

Acknowledgments

Appendix A. Supplementary data

Supplementary material related to this article can be found, in the online version, at doi:https://doi.org/10.1016/j.apcatb.2018.12.049.

References

[1] P. Xu, G.M. Zeng, D.L. Huang, C.L. Feng, S. Hu, M.H. Zhao, C. Lai, Z. Wei, C. Huang, G.X. Xie, Z.F. Liu, Sci. Total Environ. 424 (2012) 1–10.

[2] X. Ren, G. Zeng, L. Tang, J. Wang, J. Wan, Y. Liu, J. Yu, H. Yi, S. Ye, R. Deng, Sci. Total. Environ. 610-611 (2018) 1154–1163.

[3] M. Cheng, G. Zeng, D. Huang, C. Lai, P. Xu, C. Zhang, Y. Liu, Chem. Eng. J. 284 (2016) 582–598.

[4] M. Chen, P. Xu, G. Zeng, C. Yang, D. Huang, J. Zhang, Biotechnol. Adv. 33 (2015) 745–755.

[5] J. Liang, Z. Yang, L. Tang, G. Zeng, M. Yu, X. Li, H. Wu, Y. Qian, X. Li, Y. Luo, Chemosphere 181 (2017) 281–288.

[6] W.W. Tang, G.M. Zeng, J.L. Gong, J. Liang, P. Xu, C. Zhang, B.B. Huang, Sci. Total. Environ. 468-469 (2014) 1014–1027.

[7] H. Wu, C. Lai, G. Zeng, J. Liang, J. Chen, J. Xu, J. Dai, X. Li, J. Liu, M. Chen, L. Lu, L. Hu, J. Wan, Crit. Rev. Biotechnol. 37 (2017) 754–764.

[8] W. Xue, D. Huang, G. Zeng, J. Wan, C. Zhang, R. Xu, M. Cheng, R. Deng, J. Hazard. Mater. 341 (2017) 381–389.

[9] Z. Wei, M. Liu, Z. Zhang, W. Yao, H. Tan, Y. Zhu, Energ. Environ. Sci. 11 (2018) 2581–2589.

[10] Y. Zheng, Z. Yu, H. Ou, A.M. Asiri, Y. Chen, X. Wang, Adv. Funct. Mater. 28 (2018) 1705407.

[11] M. Cheng, C. Lai, Y. Liu, G. Zeng, D. Huang, C. Zhang, L. Qin, L. Hu, C. Zhou, W. Xiong, Coord. Chem. Rev. 368 (2018) 80–92.

[12] M. Cheng, G. Zeng, D. Huang, C. Lai, Y. Liu, C. Zhang, J. Wan, L. Hu, C. Zhou, W. Xiong, Water Res. 138 (2018) 7–18.

[13] Y. Yang, C. Zhang, C. Lai, G. Zeng, D. Huang, M. Cheng, J. Wang, F. Chen, C. Zhou, W. Xiong, Adv. Colloid Interface Sci. 254 (2018) 76–93.

[14] H. Yi, D. Huang, L. Qin, G. Zeng, C. Lai, M. Cheng, S. Ye, B. Song, X. Ren, X. Guo, Appl. Catal. B: Environ. 239 (2018) 408–424.

[15] Y. Lin, S. Wu, X. Li, X. Wu, C. Yang, G. Zeng, Y. Peng, Q. Zhou, L. Lu, Appl. Catal. B: Environ. 227 (2018) 557–570.

[16] Y. Shiraishi, S. Kanazawa, Y. Sugano, D. Tsukamoto, H. Sakamoto, S. Ichikawa, T. Hirai, ACS Catal. 4 (2014) 774–780.

[17] H. Wang, X. Sun, D. Li, X. Zhang, S. Chen, W. Shao, Y. Tian, Y. Xie, J. Am. Chem. Soc. 139 (2017) 2468–2473.

[18] H. Wang, S. Jiang, S. Chen, X. Zhang, W. Shao, X. Sun, Z. Zhao, Q. Zhang, Y. Luo, Y. Xie, Chem. Sci. 8 (2017) 4087–4092.

[19] J. Chen, C.L. Dong, D. Zhao, Y.C. Huang, X. Wang, L. Samad, L. Dang, M. Shearer, S. Shen, L. Guo, Adv. Mater. 29 (2017) 1606198.

[20] G. Zhang, G. Li, Z.A. Lan, L. Lin, A. Savateev, T. Heil, S. Zafeiratos, X. Wang, M. Antonietti, Angew. Chem. Int. Ed. Engl. 56 (2017) 13445–13449.

[21] W.J. Ong, L.L. Tan, H.N. Yun, S.T. Yong, S.P. Chai, Chem. Rev. 116 (2016) 7159–7329.

[22] D. Huang, X. Yan, M. Yan, G. Zeng, C. Zhou, J. Wan, M. Cheng, W. Xue, ACS Appl. Mater. Inter. 10 (2018) 21035–21055.

[23] J. Hu, C. Yu, C. Zhai, S. Hu, Y. Wang, N. Fu, L. Zeng, M. Zhu, Catal. Today 315 (2018) 36–45.

[24] M. Zhu, C. Zhai, M. Sun, Y. Hu, B. Yan, Y. Du, Appl. Catal. B: Environ. 203 (2017) 108–115.

[25] Y. Wang, W. Yang, X. Chen, J. Wang, Y. Zhu, Appl. Catal. B: Environ. 220 (2018) 337–347.

[26] J. Xu, L. Zhang, R. Shi, Y. Zhu, J. Mater. Chem. A 1 (2013) 14766–14772.

[27] N. Tian, Y. Zhang, X. Li, K. Xiao, X. Du, F. Dong, G.I.N. Waterhouse, T. Zhang, H. Huang, Nano Energy 38 (2017) 72–81.

[28] Y. Deng, L. Tang, G. Zeng, Z. Zhu, M. Yan, Y. Zhou, J. Wang, Y. Liu, J. Wang, Appl. Catal. B: Environ. 203 (2017) 343–354.

[29] C. Zhou, C. Lai, D. Huang, G. Zeng, C. Zhang, M. Cheng, L. Hu, J. Wan, W. Xiong, M. Wen, X. Wen, L. Qin, Appl. Catal. B: Environ. 220 (2018) 202–210.

[30] Q. Xiang, J. Yu, M. Jaroniec, J. Phys. Chem. C 115 (2011) 7355–7363.

[31] J. Liu, Y. Liu, N. Liu, Y. Han, X. Zhang, H. Huang, Y. Lifshitz, S.T. Lee, J. Zhong, Z. Kang, Science 347 (2015) 970–974.
[32] L. Jiang, X. Yuan, G. Zeng, Z. Wu, J. Liang, X. Chen, L. Leng, H. Wang, H. Wang, Appl. Catal. B: Environ. 221 (2018) 715–725.
[33] Q. Weng, X. Wang, X. Wang, Y. Bando, D. Golberg, Chem. Soc. Rev. 45 (2016) 3989–4012.
[34] C. Zhou, C. Lai, C. Zhang, G. Zeng, D. Huang, M. Cheng, L. Hu, W. Xiong, M. Chen, J. Wang, Y. Yang, L. Jiang, Appl. Catal. B: Environ. 238 (2018) 6–18.
[35] X. Fu, Y. Hu, Y. Yang, W. Liu, S. Chen, J. Hazard. Mater. 244-245 (2013) 102–110.
[36] C. Zhu, J. Zheng, L. Fang, P. Hu, Y. Liu, X. Cao, M. Wu, J. Mol. Catal. A: Chem. 424 (2016) 135–144.
[37] S. Haastrup, S. Latini, K. Bolotin, K.S. Thygesen, Phys. Rev. B 94 (2016) 041401.
[38] M. Liu, Y. Xu, Y. Wang, X. Chen, X. Ji, F. Niu, Z. Song, J. Liu, Adv. Mater. (Weinheim, Germany) 5 (2017) 1600661.
[39] T.G. Novak, J. Kim, S.H. Song, G.H. Jun, H. Kim, M.S. Jeong, S. Jeon, Small 12 (2016) 994–999.
[40] H. Huang, K. Xiao, N. Tian, F. Dong, T. Zhang, X. Du, Y. Zhang, J. Mater. Chem. A 5 (2017) 17452–17463.
[41] B. Huo, B. Liu, T. Chen, L. Cui, G. Xu, M. Liu, J. Liu, Langmuir 33 (2017) 10673–10678.
[42] J.-H. Deng, X.-R. Zhang, G.-M. Zeng, J.-L. Gong, Q.-Y. Niu, J. Liang, Chem. Eng. J. 226 (2013) 189–200.
[43] J.L. Gong, B. Wang, G.M. Zeng, C.P. Yang, C.G. Niu, Q.Y. Niu, W.J. Zhou, Y. Liang, J. Hazard. Mater. 164 (2009) 1517–1522.
[44] F. Long, J.-L. Gong, G.-M. Zeng, L. Chen, X.-Y. Wang, J.-H. Deng, Q.-Y. Niu, H.-Y. Zhang, X.-R. Zhang, Chem. Eng. J. 171 (2011) 448–455.
[45] Y. Yang, Z. Zeng, C. Zhang, D. Huang, G. Zeng, R. Xiao, C. Lai, C. Zhou, H. Guo, W. Xue, M. Cheng, W. Wang, J. Wang, Chem. Eng. J. 349 (2018) 808–821.
[46] C. Zhou, C. Lai, P. Xu, G. Zeng, D. Huang, Z. Li, C. Zhang, M. Cheng, L. Hu, J. Wan, F. Chen, W. Xiong, R. Deng, ACS Sustain. Chem. Eng. 6 (2018) 6941–6949.
[47] W. Xiong, G. Zeng, Z. Yang, Y. Zhou, C. Zhang, M. Cheng, Y. Liu, L. Hu, J. Wan, C. Zhou, Sci. Total. Environ. 627 (2018) 235–244.
[48] M. Zhu, S. Kim, L. Mao, M. Fujitsuka, J. Zhang, X. Wang, T. Majima, J. Am. Chem. Soc. 139 (2017) 13234–13242.
[49] Z. He, C. Kim, L. Lin, T.H. Jeon, S. Lin, X. Wang, W. Choi, Nano Energy 42 (2017) 58–68.
[50] H. Guo, C.-G. Niu, L. Zhang, X.-J. Wen, C. Liang, X.-G. Zhang, D.-L. Guan, N. Tang, G.-M. Zeng, ACS Sustain. Chem. Eng. 6 (2018) 8003–8018.
[51] B. Li, C. Lai, G. Zeng, L. Qin, H. Yi, D. Huang, C. Zhou, X. Liu, M. Cheng, P. Xu,

[51] C. Zhang, F. Huang, S. Liu, ACS Appl. Mater. Interface 10 (2018) 18824–18836.
[52] H. Wang, D. Yong, S. Chen, S. Jiang, X. Zhang, W. Shao, Q. Zhang, W. Yan, B. Pan, Y. Xie, J. Am. Chem. Soc. 140 (2018) 1760–1766.
[53] W.-J. Ong, L.K. Putri, Y.-C. Tan, L.-L. Tan, N. Li, Y.H. Ng, X. Wen, S.-P. Chai, Nano Res. 10 (2017) 1673–1696.
[54] J. Wang, L. Tang, G. Zeng, Y. Deng, Y. Liu, L. Wang, Y. Zhou, Z. Guo, J. Wang, C. Zhang, Appl. Catal. B: Environ. 209 (2017) 285–294.
[55] C. Feng, Y. Deng, L. Tang, G. Zeng, J. Wang, J. Yu, Y. Liu, B. Peng, H. Feng, J. Wang, Appl. Catal. B: Environ. 239 (2018) 525–536.
[56] G. Zeng, C. Zhang, D. Huang, C. Lai, L. Tang, Y. Zhou, P. Xu, H. Wang, L. Qin, M. Cheng, Biosens. Bioelectron. 90 (2017) 542–548.
[57] C. Zhang, C. Lai, G. Zeng, D. Huang, L. Tang, C. Yang, Y. Zhou, L. Qin, M. Cheng, Biosens. Bioelectron. 81 (2016) 61–67.
[58] Y. Zhang, G.M. Zeng, L. Tang, J. Chen, Y. Zhu, X.X. He, Y. He, Anal. Chem. 87 (2015) 989–996.
[59] H. Huang, X. Li, J. Wang, F. Dong, P.K. Chu, T. Zhang, Y. Zhang, ACS Cataly. 5 (2015) 4094–4103.
[60] L.K. Putri, B.-J. Ng, W.-J. Ong, H.W. Lee, W.S. Chang, S.-P. Chai, J. Mater. Chem. A 6 (2018) 3181–3194.
[61] X. Tan, Y. Liu, G. Zeng, X. Wang, X. Hu, Y. Gu, Z. Yang, Chemosphere 125 (2015) 70–85.
[62] P. Xu, G.M. Zeng, D.L. Huang, C. Lai, M.H. Zhao, Z. Wei, N.J. Li, C. Huang, G.X. Xie, Chem. Eng. J. 203 (2012) 423–431.
[63] C. Zhang, C. Lai, G. Zeng, D. Huang, C. Yang, Y. Wang, Y. Zhou, M. Cheng, Water Res. 95 (2016) 103–112.
[64] J. Wan, G. Zeng, D. Huang, L. Hu, P. Xu, C. Huang, R. Deng, W. Xue, C. Lai, C. Zhou, K. Zheng, X. Ren, X. Gong, J. Hazard. Mater. 343 (2018) 332–339.
[65] W. Wang, P. Xu, M. Chen, G. Zeng, C. Zhang, C. Zhou, Y. Yang, D. Huang, C. Lai, M. Cheng, L. Hu, W. Xiong, H. Guo, M. Zhou, ACS Sustain. Chem. Eng. 6 (2018) 15503–15516.
[66] W.-K. Jo, S. Kumar, M.A. Isaacs, A.F. Lee, S. Karthikeyan, Appl. Catal. B: Environ. 201 (2017) 159–168.
[67] J. Cao, Z.-h. Yang, W.-p. Xiong, Y.-y. Zhou, Y.-r. Peng, X. Li, C.-y. Zhou, R. Xu, Y.-r. Zhang, Chem. Eng. J. 353 (2018) 126–137.
[68] Q. Chen, S. Wu, Y. Xin, Chem. Eng. J. 302 (2016) 377–387.
[69] J. Ma, C. Wang, H. He, Appl. Catal. B: Environ. 184 (2016) 28–34.
[70] H. Fu, C. Pan, A. Wenqing Yao, Y. Zhu, J. Phys. Chem. B 109 (2005) 22432–22439.
[71] L. Yang, G. Dong, D.L. Jacobs, Y. Wang, L. Zang, C. Wang, J. Catal. 352 (2017) 274–281.